Frequency management system (FMS) for over-the-horizon radar (OTHR) using a near-real-time ionospheric model

Thayaparan, Thayananthan; Villeneuve, Hannah; Themens, David R.; Reid, Benjamin; Warrington, Michael; Cameron, Taylor; Fiori, Robyn

DOI:
10.1109/TGRS.2022.3193015

Frequency Management System (FMS) for Over-the-Horizon Radar (OTHR) Using a Near-Real-Time Ionospheric Model

Thayananthan Thayaparan, *Senior Member, IEEE*, Hannah Villeneuve, David R. Themens, Benjamin Reid, Michael Warrington, Taylor Cameron, and Robyn Fiori

***Abstract*— Sky-wave over-the-horizon radar (OTHR) propagates radio waves off the ionosphere to provide long-range surveillance around the Earth's curvature. Frequency selection for high-latitude and polar OTHRs is challenging unless there is an environmental monitor that addresses the significant ionospheric variability in high-latitude regions, a spectrum monitor that finds unoccupied frequencies in the high-frequency (HF) radio waveband, and a frequency management system (FMS) that selects an optimal frequency from the merged results of the environmental monitor and spectrum monitor. This article describes the first FMS for high-latitude OTHR that merges results from the environmental monitor and spectrum monitor in real-time. The environmental monitor uses the assimilative Canadian high-arctic ionospheric model (A-CHAIM), which assimilates near-real-time data and is, to date, the most advanced ionospheric model for high-latitude regions. Despite remaining limitations, demonstrations of this real-time FMS between a transmitter and four targets during the day and night and during fall and summer show that it could be one of the tools for selecting frequencies for operational scenarios.**

***Index Terms*— Arctic, assimilation Canadian high-arctic ionospheric model (A-CHAIM), environmental monitor, high-frequency (HF) propagation, high-latitude, ionosphere, over-the-horizon radar (OTHR), ray-tracing, real-time frequency management system (FMS), spectrum monitor.**

I. Introduction

IN RECENT years, Canada has resumed researching sky-wave over-the-horizon radar (OTHR) with the goal of using it to perform surveillance of its Arctic regions. Sky-wave OTHR has maximum detection ranges of approximately 3000 km compared to the typical detection range for surface-wave OTHRs of 350–400 km. Sky-wave OTHR can provide coverage of large areas (i.e., with an order of magnitude of millions of square kilometers) by refracting high-frequency (HF) radio waves off the ionosphere [1]–[13].

The ionosphere is a region of the atmosphere with a high concentration of ions and electrons between approximately 50 and 500 km in altitude above the Earth's surface. The ionosphere has three main layers called the D-layer, E-layer, and F-layer. Typically, the D-layer is between 50 and 90 km in altitude, the E-layer is between 90 and 150 km in altitude, and the F-layer is 150 km in altitude and higher [14]–[16]. The ionosphere's structure changes diurnally. For example, the intensity of the D-layer diminishes significantly at night [14], [15]. The electron density in the ionosphere and ionospheric features also vary throughout the solar cycle and between seasons due to differences in how much and where ionization energy from the Sun strikes the Earth's atmosphere [14], [15].

OTHR operational parameters, namely the transmission frequency and elevation angle, must be adjusted to respond to these regular ionospheric changes. However, there are ionospheric conditions that present challenges to operating OTHRs in high-latitude regions, including northern Canada. The high-latitude ionosphere has unique structures and regions, such as the main ionospheric trough and the auroral oval [14], [15]. Additionally, several phenomena cause or result from rapid and frequent changes in electron density in the high-latitude ionosphere. These include traveling ionospheric disturbances, patches and arcs of intense electron density, and sporadic E-layers [2], [14], [17]–[21]. The variability that these phenomena introduce to the high-latitude ionosphere is significant and hampers the real-time prediction and monitoring of ionospheric conditions.

Several well-known ionospheric models, such as the international reference ionosphere (IRI) and the NeQuick models, were developed for use at midlatitudes [22], [23]. While these models work well at midlatitudes, they have decreased accuracy at high latitudes (i.e., above 50°N geomagnetic latitude) in part due to the lack of available data for northern regions [24]–[26]. The IRI has discontinuities in its derivatives globally, particularly in the morning and evening that impair ray-tracing calculations [27]. For these reasons, Defense Research and Development Canada (DRDC) funded the development of several Canadian high-arctic ionospheric models (CHAIMs) through the University of New Brunswick's Radio Physics Laboratory under the all domain situational awareness (ADSA) program. The empir-

Manuscript received 12 April 2022; revised 29 June 2022; accepted 14 July 2022. Date of publication 21 July 2022; date of current version 4 August 2022. The work of Benjamin Reid was supported by the Canadian Space Agency (CSA) under Grant 21SUSTCHAI. *(Corresponding author: Thayananthan Thayaparan.)*

Thayananthan Thayaparan and Hannah Villeneuve are with the Defense Research and Development Canada, Ottawa, ON K2K 2Y7, Canada (e-mail: thayananthan.thayaparan@drdc-rddc.gc.ca).

David R. Themens is with the School of Engineering, University of Birmingham, Birmingham B15 2TT, U.K.

Benjamin Reid is with the Department of Physics, University of New Brunswick, Fredericton, NB E3B 5A3, Canada.

Michael Warrington is with the Department of Engineering, University of Leicester, Leicester LE1 7RH, U.K.

Taylor Cameron and Robyn Fiori are with Natural Resources Canada, Ottawa, ON K1A 0E4, Canada.

Digital Object Identifier 10.1109/TGRS.2022.3193015

ical CHAIM (E-CHAIM) [28]–[30] preceded the creation of assimilative CHAIM (A-CHAIM) [27], [31]. A-CHAIM assimilates near-real-time ionospheric data into a background produced by E-CHAIM [31]. The new A-CHAIM model is the most advanced ionospheric model for high-latitude and polar regions and makes use of a particle filter assimilation method rather than conventional Kalman filters or variational approaches [31]. A-CHAIM does not have discontinuities in its electron density profile [28]. A-CHAIM will be used in this article to find operational frequencies and elevation angles for an OTHR.

The OTHR is not an allocated user of the HF band in which it operates, so the spectrum must be constantly monitored to find unoccupied frequencies. Because of the constraints posed by ionospheric conditions and occupied or forbidden channels in the HF band, it is crucial to have a frequency management system (FMS) that can quickly find suitable operational parameters for OTHR in high-latitude regions [26]. This article presents the first FMS that works in real-time and is suitable for use in high-latitude and polar regions. Section II explains how the real-time FMS works, Section III presents the results and covers the FMS's limitations, and Section IV offers some conclusions.

II. Methodology

The FMS is comprised of two subsystems: the environmental monitor, which determines which frequencies would allow the OTHR to operate based on ionospheric conditions, and the spectrum monitor, which determines which frequencies are unoccupied and checks if frequencies are not on a list of forbidden frequencies. The monitors are run separately but at the same time. The environmental monitor typically updates every 15 min or less, and the spectrum monitor updates every second. The FMS merges the outputs of the monitors every second (i.e., when either or both monitors update). Section II-A describes the spectrum monitor, Section II-B describes the environmental monitor, and Section II-C describes how the real-time FMS will be demonstrated.

A. Spectrum Monitor

The spectrum monitor is necessary because OTHR is not an allocated user of the HF band and must not interfere with other users or allocated radio-frequency services. The methodology of the spectrum monitor involves removing headers from and reading the data from SpectraVue output files into a MATLAB matrix, removing impulse noise, performing power spectra averaging, performing thresholding, and making decisions about whether or not the frequency is occupied. SpectraVue software [32] monitors the frequency spectrum from 2 to 22 MHz with a resolution of 1.22 kHz. It collects power spectra data every second, but the spectrum monitor requires data from the previous 60 consecutive seconds. As such, the spectrum monitor must be run for at least 1 min before it can be used in the FMS. Impulse noise is short-lived noise (e.g., nearly instantaneous) that is intense compared to the background noise [33]. There are many causes of impulse noise, but one example is lightning [33]. To remove impulse noise, any power spectra with amplitudes greater than 10 dB above the median noise floor are discarded. The median noise floor was estimated using erode and dilate processing [34]. Then, the spectrum is averaged and the noise floor is found again. Any power spectra averaged over a minute with amplitudes more than 6 dB above the noise floor are considered occupied and assigned an occupancy state vector with a value of 1. Any averaged power spectra less than 6 dB above the noise floor are considered unoccupied and assigned an occupancy state vector with a value of 0. Industry Canada recommended using 6 dB above the noise floor as a threshold for determining occupancy without too many false positives. Forbidden frequencies are frequencies that Industry Canada reserved for allocated users, so the spectrum monitor always assigns forbidden frequencies with occupancy state vectors with the value of 1. Each averaged power spectrum has one occupancy state vector per frequency per second. After there are occupancy state vector data for the preceding 60 seconds, M of N filtering is used to refine the determination of occupancy. In M of N filtering, if at least 30 (i.e., M) out of the 60 (i.e., N) occupancy state vectors examined at any given moment have a value of 1, then the frequency is considered to be occupied. The spectrum monitor examines a 10-kHz wide channel centered around each frequency and considers the entire channel as occupied if any frequency within it is occupied [35], [36].

B. Environmental Monitor

DRDC funded the first of the high-latitude ionospheric models, E-CHAIM, which was developed by the University of New Brunswick's Radio Physics Laboratory [28]–[30]. E-CHAIM generally had higher accuracy than traditional models but insufficiently modeled short-term ionospheric events and variability in the ionosphere due to its empirical nature [27], [37], [38]. A-CHAIM is the second of the CHAIM models and assimilates near-real-time ionospheric data into a background created by E-CHAIM. Several comparisons verified that A-CHAIM usually models the ionosphere better than E-CHAIM [27], [31]. As a result, A-CHAIM is being used in this environmental monitor.

The version of A-CHAIM used in this demonstration (Version 2.0) underwent two main stages of development. First, the main A-CHAIM was developed. Later, an E-region auroral precipitation model was added to A-CHAIM [39]. This precipitation model is the same as in [39] except that it assimilates data from the Defense Meteorological Satellite Program's Special Sensor Ultraviolet Spectrographic Imager. A-CHAIM uses near-real-time data from the Poker Flats incoherent scatter radar, ground- and satellite-based Global Navigation Satellite System (GNSS) receivers, the Defense Meteorological Satellite Program's Special Sensor Ultraviolet Spectrographic Imager, altimeters on satellites, and Global Ionospheric Radio Observatory ionosondes [39], [40]. The ionosondes give data on the vertical electron density profile up to hmF2 (i.e., the altitude of the peak electron density in the F2-layer). The near-real-time ionosonde data

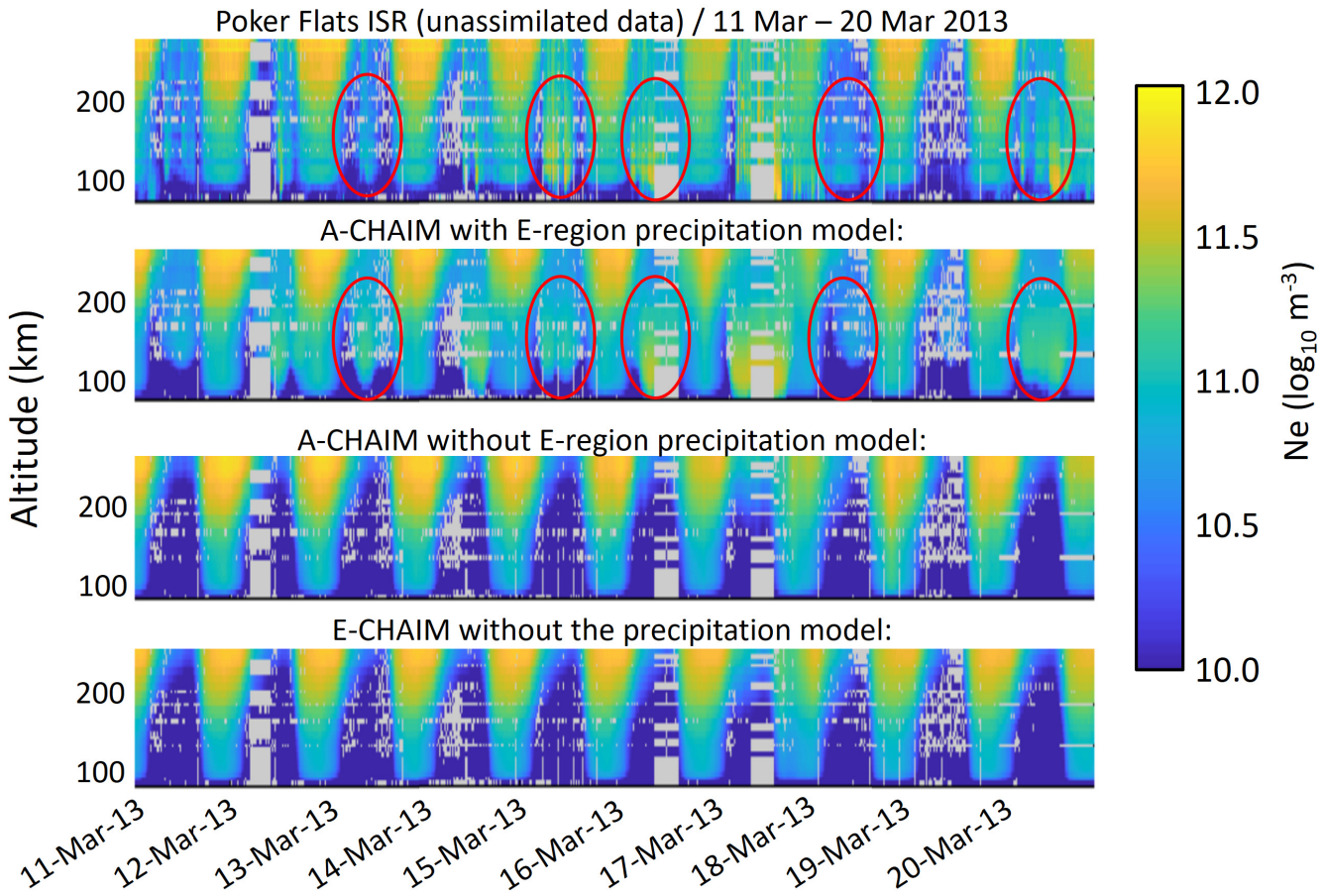

Fig. 1. (Top) Vertical electron density profile from incoherent scatter radar data. (Second) A-CHAIM with the E-layer precipitation model. (Third) A-CHAIM without the precipitation model. (Bottom) E-CHAIM without the precipitation model. The effect of the A-CHAIM precipitation model is most pronounced below 200 km on March 13, 15, 16, 18, and 20, shown in the red circles. This figure should be interpreted as an example, rather than validation, of the precipitation model [39], [40].

for A-CHAIM are scaled automatically using an automatic real-time ionogram scalar with true height (ARTIST) software. The satellite-borne altimeters measure the vertical total electron density in the ionosphere above the oceans and are handled similar to the GNSS data [27].

A-CHAIM models the vertical electron density profile using the same functional form as E-CHAIM, where the system adjusts hmF2, the critical frequency of the F-layer (foF2), and the topside and bottomside thicknesses of the background model to better reflect measured behaviors. Horizontal variability in A-CHAIM is represented by spherical cap harmonics, with each vertical parameter represented by a separate set of harmonics [27]. While the environmental monitor would ideally update every 5 min to account for rapid ionospheric changes, the output files from A-CHAIM were only available in 15-min intervals for the dates in this study. Currently, A-CHAIM generates output files at 5-min intervals, so the environmental monitor can now have an update time of approximately 5 min depending on the resolution of the ray-tracing parameters and the available computing power. Every hour, A-CHAIM's assimilation system collects and processes all available data from the previous 3 h and conducts a 2-h persistence forecast. This means that any given time has five potential assimilation outputs: 2–3, 1–2, or 0–1 h hindcast and a 0–1 or 1–2 h forecast. In this study, the 3-h hindcast output was used as hindcasts are generally more accurate than forecasts [31].

While Fig. 1 is not meant to be interpreted as a validation, it shows an example comparison of the E-layer precipitation model for A-CHAIM, where the A-CHAIM system was run for a historical event, imposing the same data latency or availability behavior of the real system [39]. A-CHAIM, with and without the inclusion of precipitation, were compared to the default E-CHAIM output [39]. Fig. 1 shows that A-CHAIM had improvements when its precipitation model was included, particularly during the nights (e.g., March 13, 15, 16, 18, and 20) between altitudes of 100 and 175 km and storm events circled in red. Overall, A-CHAIM with the E-layer precipitation model behaved stably.

After A-CHAIM models the ionosphere, ray-tracing is performed through the ionosphere using the High-Latitude Ionospheric Propagation Laboratory (HIPLAB) ray-tracer. The University of Leicester developed HIPLAB with funding and support from DRDC [41]. HIPLAB uses the ray-tracer of Zaalov *et al.* (2003, 2005) [42], [43] and of Warrington *et al.* (2012, 2016) [44], [45], which is a modified version of Jones

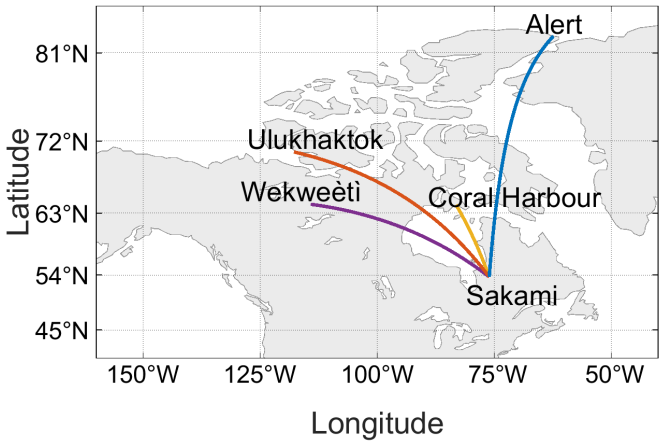

Fig. 2. Locations of the transmitter at Sakami and the four targets at Coral Harbor, Wekweètì, Ulukhaktok, and Alert. Lines represent great circle tracks. The Miller cylindrical projection was used.

and Stephenson's ray-tracer [46]. The Jones and Stephenson ray-tracer uses the Appleton–Hartree formula to calculate the refractive index. Ray-tracing requires the integration of a system of Haselgrove differential equations to account for the changing refractive index in the temporally and anisotropically varying ionosphere.

C. Demonstration of the Real-Time FMS

Because this is a demonstration of the FMS and not the OTHR, the OTHR was not physically operated during this demonstration. The transmitter and target locations in the presented simulation case study do not correspond to actual transmitters or receivers. The list of forbidden frequencies used in the spectrum monitor is a simulated list generated with pseudorandom intervals of frequencies that may not be used for simulated OTHR operation. However, the ionospheric data supplied to the A-CHAIM portion of the environmental monitor and the spectral data supplied to the spectrum monitor were real, measured data.

In this demonstration, the transmitter was at Sakami (53.70°N, 76.07°W). The four targets arranged from closest to farthest from the transmitter were at Coral Harbor (64.14°N, 83.17°W), Wekweètì (64.19°N, 114.18°W), Ulukhaktok (70.74°N, 117.78°W), and Alert (82.5°N, 62.35°W), as shown in Fig. 2. The great circle distances between the transmitter and targets were 1230 km to Coral Harbor, 2430 km to Wekweètì, 2780 km to Ulukhaktok, and 3240 km to Alert. The local time zones were coordinated universal time (UTC)-4h for Sakami, UTC-5h for Coral Harbor, UTC-6h for Wekweètì, UTC-6h for Ulukhaktok, and UTC-4h for Alert. The FMS was demonstrated for two consecutive times for a fall day [October 11, 2020, at 17:07:30 (UTC) and 17:22:30 (UTC)], a fall night [October 11, 2020, at 05:07:30 (UTC) and 05:22:30 (UTC)], a summer day [June 21, 2021, at 17:07:30 (UTC) and 17:22:30 (UTC)], and a summer night [June 21, 2021, at 05:07:30 (UTC) and 05:22:30 (UTC)]. The current experimental OTHR being designed at DRDC has an 8×8 planar array of monopoles, each of which is omnidirectional, for transmission and 16×16 array for the reception. Each of the 64 transmit antennas can be excited with independent waveforms at 64 kW peak power and up to 100% duty cycle. The operating frequency is 3–18 MHz. The pulse repetition frequency (PRF) is 25–50 Hz and the coherent pulse integration (CPI) is 20 s. Furthermore, the antenna beamwidth is approximately 20–30°. The antenna beam can be steered to arbitrary azimuth (0–360°) and elevation (0–90°) angles. In the next phase of the project, the transmit array and receive array will be expanded to a 16×16 array and a 32×32 array, respectively. More detailed descriptions of the system can be found in [12], [47], [48].

HIPLAB simulated the OTHR operation because it traced paths that HF radio waves would likely take through the ionosphere. HIPLAB was run for frequencies between 1 and 22 MHz with a frequency step of 0.1 MHz and elevation angles between 1° and 60° with an elevation angle step of 0.1°. The azimuth range provided to HIPLAB was 15° with a step of 0.4°, so rays were sent up to 7.5° to the left and the right of the great circle path between the transmitter and target.

Rays landing within a 50-km radius of the target were considered to have been received. The power density on the ground surrounding the receiver was calculated by assigning a signal power contribution to each ray based on the transmitter power, transmitter antenna gain, D-region absorption, and the geometry of the distribution of rays on a spherical surface around the transmit antenna. The received signal power was then determined from the power density incident on the receiver antenna taking the antenna gain into account. To calculate the signal-to-noise ratio (SNR), the noise floor was estimated based on the International Telecommunication Union (ITU) recommendation on radio noise [49] and compared to the received signal power. Frequency and elevation angle pairs were ranked according to the associated SNR values. Generally, the constraints posed by the environmental monitor were more restrictive than the constraints from the spectrum monitor. For this reason, the results of the environmental monitor were examined more closely.

III. Results and Discussion

Section III-A discusses the results of the environmental monitor in greater detail, Section III-B analyzes the results of the spectrum monitor and FMS as a whole, and Section III-C discusses the limitations and future work for the FMS.

A. Output of the Environmental Monitor, Including the Output From A-CHAIM and HIPLAB

Fig. 3 shows the maximum critical frequency of the ionosphere modeled by A-CHAIM over the polar cap for the eight times in the demonstration mentioned in Section II-C. The critical frequency is the largest frequency where radio waves can reflect off of the ionosphere rather than pass through the ionosphere to escape to outer space. The main ionospheric trough, shown as the dark blue arc where there is a lower electron density, appeared in the nighttime side of the polar cap in the plots for the fall nighttime, fall daytime, and summer nighttime. The ionospheric plots for the fall times changed minimally between the 15-min intervals, but the plots for the

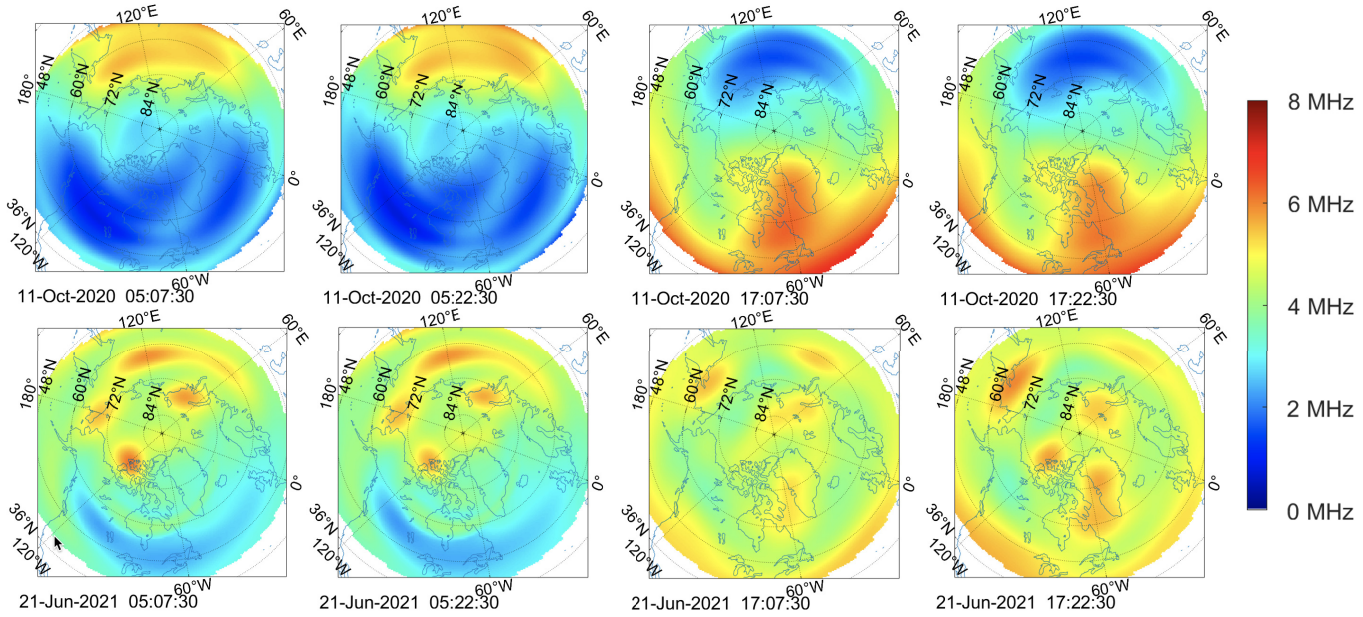

Fig. 3. Plot of maximum critical frequency (MHz) in the ionosphere modeled by A-CHAIM for the eight times. The top row shows the ionosphere on October 11, 2020, at 05:07:30 (fall night), 05:22:30 (fall night), 17:07:30 (fall day), and 17:22:30 (fall day), going from left to right. The bottom row shows the ionosphere on June 21, 2021, at 05:07:30 (summer night), 05:22:30 (summer night), 17:07:30 (summer day), and 17:22:30 (summer day), going from left to right. All times are in UTC. There were noticeable changes to the critical frequency even between the 15 min intervals.

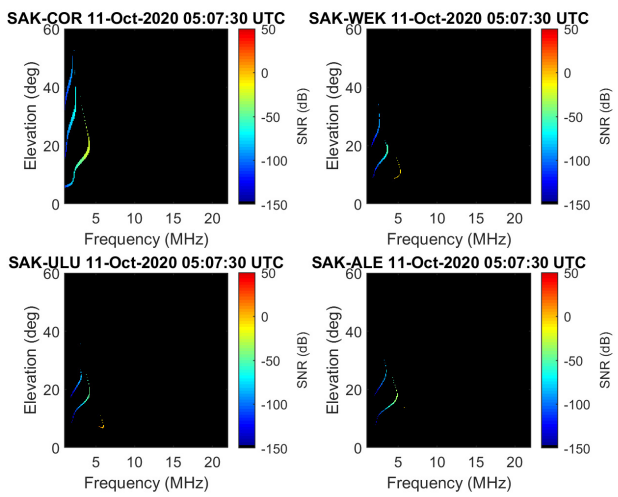

Fig. 4. Frequency-elevation bands for a fall night [October 11, 2020, at 05:07:30 (UTC)] between the transmitter at Sakami and each target. The targets are Coral Harbor at the top left, Wekweètì at the top right, Ulukhaktok at the bottom left, and Alert at the bottom right. Data were from A-CHAIM and HIPLAB.

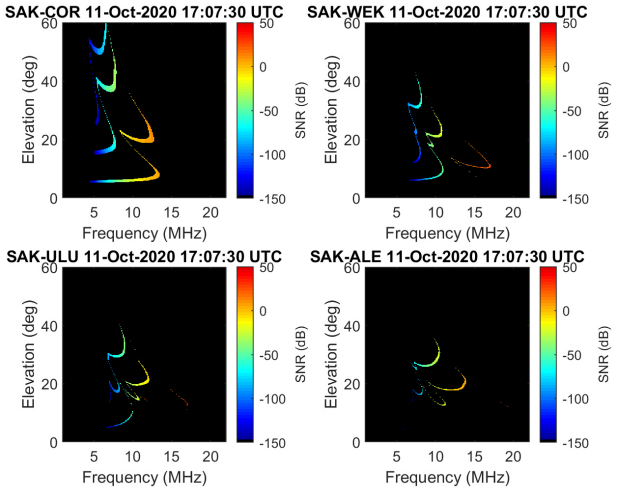

Fig. 5. Frequency-elevation bands for a fall day [October 11, 2020, at 17:07:30 (UTC)] between the transmitter at Sakami and each target. The targets are Coral Harbor at the top left, Wekweètì at the top right, Ulukhaktok at the bottom left, and Alert at the bottom right. Data were from A-CHAIM and HIPLAB.

summer daytime showed that the distribution and intensity of electron density could change significantly within a 15-min interval. The ionospheric electron density plots showed that A-CHAIM could model subtle short-term changes at high latitudes. Ray-tracing typically took less time for the nighttime than for the daytime for both seasons because the weaker nightside ionosphere resulted in more rays escaping to space.

Figs. 4–7 show the frequency-elevation bands (i.e., SNR versus frequency and elevation angle) for the four targets. The frequency-elevation bands typically looked like backward c's or streaks. There typically was one frequency-elevation band corresponding to a certain number of hops that rays took between the ground and an ionospheric layer as long as the SNR was sufficient to show up on the plot. For example, there could be a band for rays that propagated with two hops off the E-layer, another for rays that propagated with one hop off the F-layer, and so on. The frequency-elevation bands generally became less cohesive or had weaker SNR when the target was increasingly farther from the transmitter. The latter tendency was likely due to signal attenuation (e.g., free

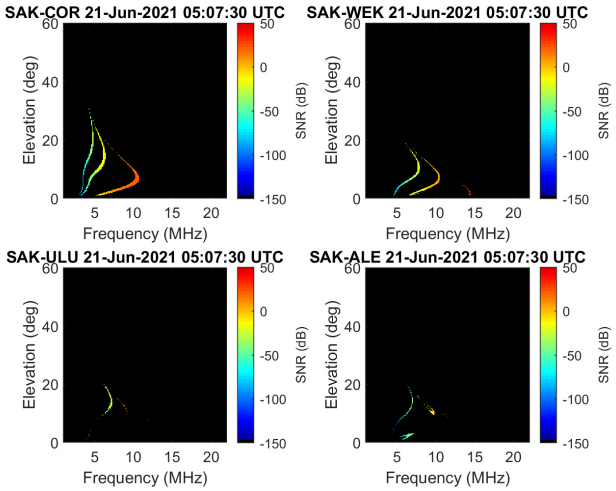

Fig. 6. Frequency-elevation bands for a summer night [June 21, 2021, at 05:07:30 (UTC)] between the transmitter at Sakami and each target. The targets are Coral Harbor at the top left, Wekweètì at the top right, Ulukhaktok at the bottom left, and Alert at the bottom right. Data were from A-CHAIM and HIPLAB.

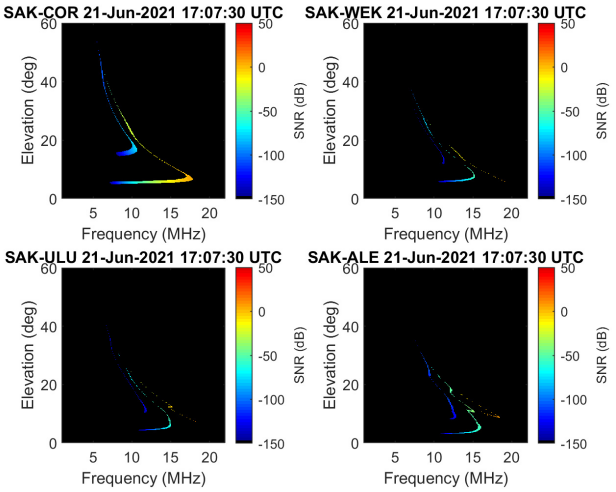

Fig. 7. Frequency-elevation bands for a summer day [June 21, 2021, at 17:07:30 (UTC)] between the transmitter at Sakami and each target. The targets are Coral Harbor at the top left, Wekweètì at the top right, Ulukhaktok at the bottom left, and Alert at the bottom right. Data were from A-CHAIM and HIPLAB.

space path loss, absorption, etc.) or off-great circle propagation due to ionospheric features [50]. There were also fewer rays aimed directly at the radius around the farther targets because the radius size did not increase proportionally with distance from the transmitter due to the constant azimuth angle range. However, the less cohesive frequency-elevation bands for farther targets typically had a similar frequency range overall when compared to closer targets, as illustrated in Fig. 9. The number, shape, and strength of the bands changed diurnally and seasonally. The bands were smaller and had less frequency spread at night compared to during the day.

Each plot had at least one notable feature. The explanations of these features were informed by plots of the vertical trajectories of rays. Fig. 8 shows the vertical trajectories of rays

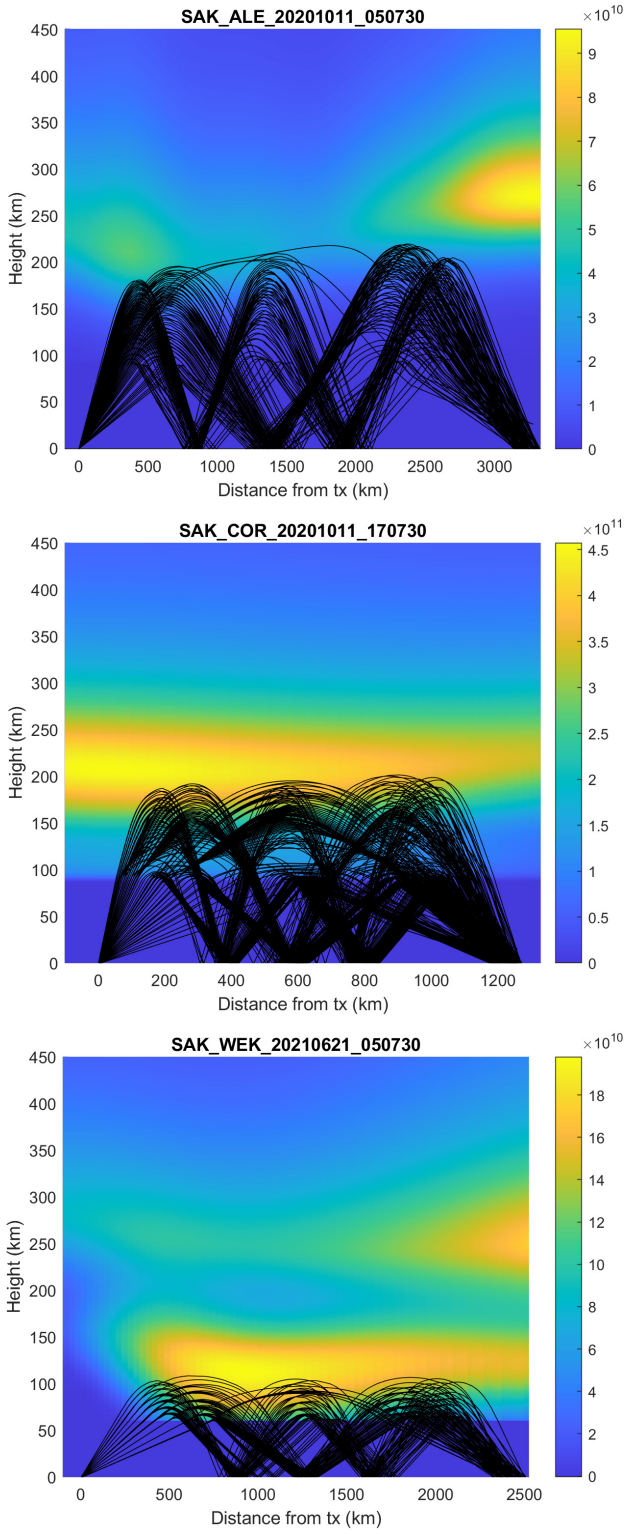

Fig. 8. (Top) Vertical ray trajectories between Sakami and Alert on October 11, 2020, at 05:07:30 (UTC). (Middle) Coral Harbor on October 11, 2020, at 17:07:30 (UTC). (Bottom) Wekweètì on June 21, 2021, at 05:07:30 (UTC). The background shows a vertical "slice" of ionospheric electron density. The colorbar's unit is electrons per cubic meter. A fraction of the rays that landed within 50 km of the target were plotted to avoid crowding the figure.

that landed within 50 km of the target against a background of a vertical "slice" of ionospheric electron density for one target each on October 11, 2020, at 05:07:30 (UTC) and

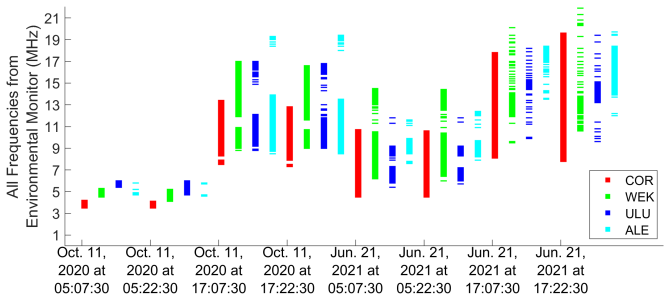

Fig. 9. Frequencies of rays with SNRs of at least −20 dB for each target on a fall night (October 11, 2020, at 05:07:30 and 05:22:30), a fall day (October 11, 2020, at 17:07:30 and 17:22:30), a summer night (June 21, 2021, at 05:07:30 and 05:22:30), and a summer day (June 21, 2021, at 17:07:30 and 17:22:30). (Red) "COR" corresponds to Coral Harbor. (Green) "WEK" corresponds to Wekweètì. (Blue) "ULU" corresponds to Ulukhaktok. (Cyan) "ALE" corresponds to Alert. All times are in UTC.

17:07:30 (UTC) and on June 21, 2021, at 05:07:30 (UTC). Fig. 4 for October 11, 2020, at 05:07:30 (UTC) had three small frequency-elevation bands for the closest three targets but only two for the farthest target at Alert. An examination of the vertical trajectory plots showed that all targets had one-, two-, and three-hop propagation, though the top subplot in Fig. 8 showed that Alert had very little one-hop propagation. Each target had two- and three-hop propagation from both the E- and F-layers. Coral Harbor had one hop propagation from both the E- and F-layers, but the farthest three targets only had one hop propagation off the F-layer. Despite at least five propagation paths available for each target, the even distribution of ray reflection heights between the E- and F-layers resulted in only one band for two-hop propagation and one band for three-hop propagation. The distribution was even because there was no E-F valley at this time between the extremely weak E-layer and relatively stronger F-layer.

In Fig. 5 for October 11, 2020, at 17:07:30 (UTC), the frequency-elevation bands for Coral Harbor had larger elevation angles (e.g., approaching 60°) compared to the other targets at this time and at other times. The Coral Harbor target had six frequency-elevation bands, which was a larger number than any other target at all times in this study. The six bands were from one-, two-, and three-hop propagation from both the E- and F-layers, as shown in the middle subplot in Fig. 8. Alert was the farthest target and had only four bands that were diminished and less cohesive in Fig. 5. Fig. 6 for June 21, 2021, at 05:07:30 (UTC) had three frequency-elevation bands for the Coral Harbor and Wekweètì targets but fewer bands for Ulukhaktok and Alert than in Fig. 4, which was also at nighttime. The bottom subplot in Fig. 8 showed that there was mainly two- and three-hop propagation off the E-layer, and these rays covered a nearly identical range in outgoing elevation angles. The few rays with one-hop propagation had a low elevation angle, which corresponds to the right-most frequency-elevation band on each subplot in Fig. 6. While there was relatively less one-hop propagation, the SNR was adequate for these rays according to Fig. 6. The bands in Fig. 6 reached higher maximum frequencies than in Fig. 4 and mainly corresponded to an auroral-E propagation mode [51]. Coral Harbor had a frequency-elevation band with unusually high SNR around 8–11 MHz. The lower portions of the bands in Fig. 6 were sloped almost vertically, similar to Fig. 4 but dissimilarly to the more horizontal lower portions of the daytime bands in Figs. 5 and 7. This indicates that a wide range of elevation angles worked for a relatively small frequency range during the nights.

In Fig. 7 for June 21, 2021, at 17:07:30 (UTC), there were two bands for the closest target and three bands for the farthest three targets. These bands were very narrow and had very weak SNR values, so they are best viewed when magnified. While the vertical ray trajectory plots showed that there was one-, two-, and three-hop propagation off one ionospheric layer for all four targets, some propagation paths did not yield sufficient SNR to appear in Fig. 7 for the first target. The top portions of the bands nearly overlapped but had significantly different SNRs. Generally, the bands at higher frequencies had higher SNRs than bands at lower frequencies at the same time.

Fig. 9 shows the frequencies of rays that had SNRs of at least −20 dB from the output of the HIPLAB ray-tracer. While a negative SNR is insufficient for target detection, target detection is not the focus of this study. Additionally, real operational scenarios could improve the SNR level for these frequencies by optimizing radar parameters, such as the configuration, number, and power of the transmitter antennas [48], [52], [53]. Some general conclusions can be found from Fig. 9: the frequencies were lower at the night [05:07:30 and 05:22:30 (UTC)] than during the day [17:07:30 and 17:22:30 (UTC)], and the frequencies on a fall night (October 11, 2020) were very close to the lower end of the HF range compared to any other time in the demonstration. The usable frequency range on a fall night was restricted for all targets because the maximum usable frequency was lower when the ionospheric electron density was lower.

B. Output of the FMS After Merging

Fig. 10 shows the measured, forbidden, unoccupied, ray-traced, and advised frequencies across part of the HF spectrum for the Coral Harbor target at night [05:07:30 (UTC)] and during the day [17:07:30 (UTC)] on October 11, 2020. The amplitude in Fig. 10 is from the spectrum monitor and is completely independent of the SNR from the environmental monitor. There are more frequencies shown in Fig. 10 compared to Figs. 7–9 because all frequencies that hit the target were given to the spectrum monitor regardless of SNR.

The signal power as measured by the spectrum monitor varied across the spectrum. Even though there were few frequencies available based on the ray-tracing results for the night, there were still enough advised frequencies from which to choose. For both the night and the day, the majority of the ray-traced frequencies were available for use after merging. This shows that the results of the environmental monitor impacted the selection of frequencies for the OTHR more than the spectrum monitor's criteria. There were many more advised frequencies available during the day compared to the night. This result makes sense because Fig. 3 showed the ionosphere had a relatively high critical frequency between

TABLE I

TOP FIVE FREQUENCY AND ELEVATION ANGLE PAIRS FOR EACH TARGET AND TIME RANKED BY SNR (dB). THE FREQUENCIES WERE INCLUDED IN THE LIST OF ADVISED FREQUENCIES AFTER MERGING. ALL TIMES ARE IN UTC. "FREQ" IS FREQUENCY, 'EL" IS ELEVATION ANGLE, "COR" IS CORAL HARBOR, "WEK" IS WEKWEÈTÌ, "ULU" IS ULUKHAKTOK, AND "ALE" IS ALERT

	COR			WEK			ULU			ALE		
Date	**Freq. (MHz)**	**El. (°)**	**SNR**	**Freq. (MHz)**	**El. (°)**	**SNR**	**Freq. (MHz)**	**El. (°)**	**SNR**	**Freq. (MHz)**	**El. (°)**	**SNR**
Oct. 11, 2020 at 05:07:30	4.2	20.6	-3.29	4.5	8.7	17.53	5.4	7.3	26.80	4.8	19.6	-15.90
	4.2	20.7	-3.29	4.5	8.8	17.11	5.4	7.4	25.14	4.9	18.2	-16.01
	4.2	20.3	-3.34	5.1	9.6	14.60	5.8	6.8	22.25	4.9	18.1	-16.06
	4.2	20.4	-3.37	5.2	10.0	14.46	5.8	6.9	22.10	4.8	17.4	-16.11
	4.2	20.5	-3.38	4.6	8.8	13.45	5.8	7.0	21.00	4.9	18.0	-16.21
Oct. 11, 2020 at 05:22:30	4.0	22.0	-4.16	4.8	8.9	13.29	4.9	4.4	20.44	5.8	12.3	12.13
	4.0	22.3	-4.45	4.9	9.1	12.95	4.8	4.4	18.26	4.6	20.3	-19.07
	4.0	21.9	-4.49	5.1	9.7	12.04	5.8	5.8	15.42	4.6	20.4	-19.25
	4.0	22.2	-4.49	5.1	9.8	11.37	5.8	4.5	14.71	4.6	16.8	-19.42
	4.0	22.1	-4.52	4.6	8.6	11.22	5.8	4.6	14.45	4.6	16.7	-19.51
Oct. 11, 2020 at 17:07:30	12.3	22.5	28.41	17.0	10.7	42.62	17.0	11.3	62.57	10.7	18.3	2.16
	12.3	22.6	28.37	17.0	10.8	42.49	17.0	11.2	61.46	10.7	18.2	2.11
	12.2	23.4	28.31	17.0	10.9	42.42	17.0	13.0	48.24	10.5	18.4	2.00
	12.3	23.1	28.27	17.0	11.1	42.36	17.0	13.1	48.01	10.6	18.3	1.42
	12.2	23.0	28.26	17.0	11.0	42.35	17.0	12.6	47.58	10.5	15.7	1.41
Oct. 11, 2020 at 17:22:30	11.5	23.8	26.11	14.9	6.3	40.49	13.0	11.5	39.78	10.3	17.6	-0.69
	11.5	23.9	26.07	14.9	9.9	33.92	12.6	11.9	36.29	10.4	17.5	-1.20
	11.5	23.7	25.95	14.8	9.8	33.69	14.8	16.3	27.62	10.4	17.6	-1.25
	11.5	24.2	25.85	14.5	10.0	33.30	14.6	16.7	27.00	10.2	17.7	-1.52
	11.5	24.3	25.82	14.8	6.5	33.28	11.0	14.2	20.73	10.3	17.7	-1.94
Jun. 21, 2021 at 05:07:30	10.5	6.1	40.35	13.5	4.5	41.13	9.2	10.0	35.49	9.3	10.8	11.03
	10.5	6.2	40.24	13.4	4.7	40.17	9.2	10.1	29.54	9.3	10.7	10.86
	10.6	6.9	40.20	13.1	5.2	39.08	9.2	10.7	26.28	9.3	10.6	10.84
	10.6	6.3	40.16	13.0	5.4	35.55	9.2	11.1	26.43	9.2	11.0	10.50
	10.6	6.8	40.12	10.4	6.3	25.12	8.8	12.5	18.89	9.2	10.9	10.41
Jun. 21, 2021 at 05:22:30	10.5	6.3	39.91	13.5	4.2	41.22	9.2	10.4	29.07	12.3	7.9	32.40
	10.5	6.5	39.87	13.4	4.4	40.30	9.2	10.2	28.13	12.4	7.8	29.42
	10.5	6.4	39.79	13.5	4.1	38.34	9.2	10.5	26.74	9.2	10.7	10.90
	10.3	6.0	39.76	13.4	4.3	37.30	9.1	11.0	24.17	9.3	10.3	10.35
	10.5	6.6	39.74	13.1	4.9	36.17	9.1	11.2	21.45	9.3	10.4	10.26
Jun. 21, 2021 at 17:07:30	17.4	7.4	22.06	20.1	4.4	38.99	14.9	12.3	14.25	18.2	8.8	28.67
	17.4	7.3	21.97	13.5	14.2	7.16	14.8	12.3	13.72	18.2	8.9	28.41
	17.4	7.2	21.87	13.5	14.1	7.04	14.9	12.4	13.29	18.2	9.0	26.30
	17.4	7.1	21.79	13.5	14.3	6.39	14.9	12.2	13.21	17.3	9.5	26.22
	17.4	7.0	21.55	13.4	14.5	6.30	14.8	12.4	12.84	18.2	9.1	25.92
Jun. 21, 2021 at 17:22:30	18.9	7.9	26.95	21.9	4.1	41.55	14.8	13.8	13.85	17.4	11.0	24.22
	18.9	6.6	26.74	18.2	8.7	17.62	14.6	14.3	13.42	17.3	11.1	24.16
	18.9	6.5	26.69	14.6	13.7	10.38	14.5	14.6	13.27	17.0	11.3	23.25
	18.9	6.4	26.62	13.5	15.6	7.86	14.9	13.6	7.83	17.4	11.5	22.35
	18.9	6.7	26.48	13.4	16.0	6.52	14.6	14.4	12.27	17.0	11.2	21.67

the transmitter and target during the fall daytime. There are usually more ionospheric layers with higher electron densities during the day, which may "open" more propagation paths depending on their densities, altitudes, and orientations.

Table I shows the top five advised frequency and elevation angle pairs for all times in the demonstration for each target as ranked by SNR. In DRDC's operational scenarios, typically the frequency-elevation pair with the highest SNR is chosen. Most of the frequency-elevation angle pairs with the highest SNR values remained on the list of advised frequencies. Most of the targets and times had frequencies with positive SNR values.

C. Limitations and Future Work

There are limitations to this real-time FMS for high latitudes. At present, HIPLAB can model o/x polarization modes and some complex modes (e.g., off-great-circle modes due to polar patches) or multiple-mode propagation routes that are known to exist in reality. However, only the o-mode was used in this study because of computational resource constraints and because previous studies showed that o- or x-polarization resulted in the same list of usable frequencies [21], [47]. Mode complexity can complicate target detection, so ideally the mode would be a factor in selecting operational frequencies. However, HIPLAB currently ranks frequencies solely by SNR. In the future, more modes (e.g., reflections from field-aligned irregularities) and ranking based on modality could be added to HIPLAB if the computational resources can be increased. The computational power available for the FMS should also be increased to decrease the update time of the environmental monitor to approximately 5 min to address rapid ionospheric changes. At present, spread Doppler clutter is also not accounted for when ranking frequencies despite it being a prominent issue for OTHR. In the future, a spread Doppler clutter model should be added to this FMS's SNR calculation. Other transmitter antenna configurations and power are being tested with the FMS, such as a 16 by 16 array with 256 monopoles [52], [53].

A-CHAIM usually provides more accuracy compared to empirical models [27], but even so cannot capture all the variability and complexity of the real ionosphere with high

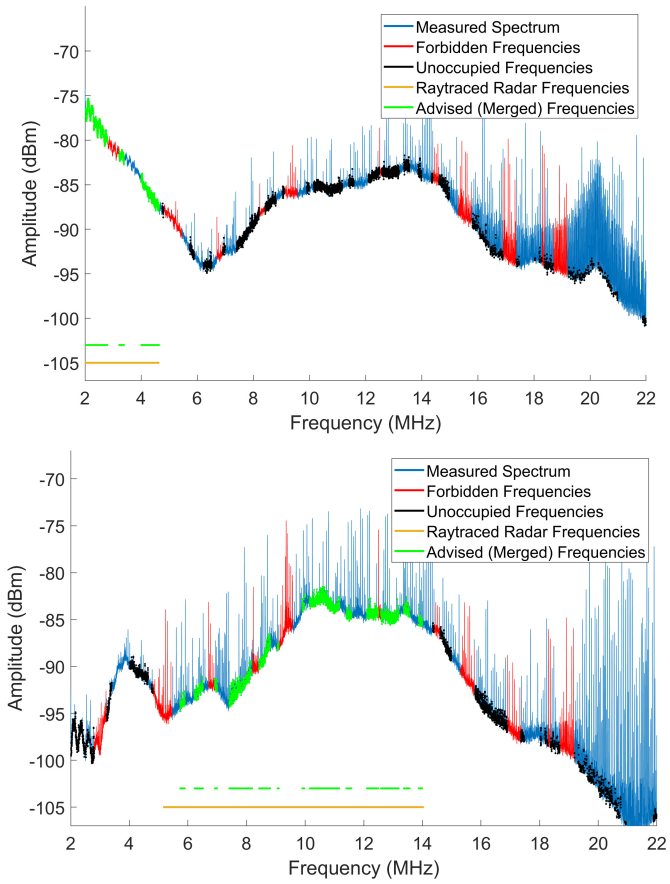

Fig. 10. Advised frequencies from the FMS (green lines) on October 11, 2020, at 05:07:30 (UTC) (top) and 17:07:30 (UTC) (bottom). The target is at Coral Harbor, so 05:07:30 (UTC) is at night and 17:07:30 (UTC) is during the day. The blue series shows the amplitude of the power spectrum averaged over a minute from the spectrum monitor. The overlaid red and black series indicate the forbidden and unoccupied frequencies, respectively. The overlaid orange and green overlaid series and horizontal lines show the ray-traced and advised frequencies, respectively, that were produced by the environmental monitor. The amplitude of the series is from the spectrum monitor and is completely independent of the SNR from the environmental monitor.

accuracy all the time. There is still not as much real-time data available at high latitudes compared to mid-latitudes. Some data sources for high latitudes, notably the Canadian Advanced Digital Ionosonde data, are not automatically scaled, so they cannot be incorporated into A-CHAIM. However, higher data availability could improve the accuracy and spatial resolution of A-CHAIM. More ionospheric sensors and instrumentation are planned for the future. A short-term forecast system with A-CHAIM is now under development, which might make OTHR operation more efficient and fine-tune the operation of the real-time FMS. Furthermore, customizable improvements can be made to A-CHAIM in the future to facilitate more focused support for an operational OTHR system, such as the inclusion of backscatter from OTHR sounding modes, the inclusion of local, higher resolution subgrid resolution in regions down-range from the radar, where scatter is available, and the ability to assimilate raw ionogram data without the need for "scaling". With the system already using a particle filter, it is incredibly fixable to the inclusion of higher nonlinear datasets, which will be an asset as a Canadian system is operationalized.

While this FMS currently can provide frequency selection guidance even with these limitations, it needs to be accompanied by other tools, such as experimental and modeled wide-sweep backscatter ionograms (WSBI), for real operational use.

IV. Conclusion

This real-time FMS for OTHR in high-latitude and polar regions worked well in the demonstration. A-CHAIM can represent the short-term variability and some unique features typical of the high-latitude ionosphere. The accuracy of A-CHAIM is due to the assimilation of near-real-time ionospheric data and the use of the E-CHAIM as the background model. The environmental monitor, which used A-CHAIM, showed that the frequency-elevation bands varied significantly on a seasonal and diurnal basis because of the variations in ionospheric conditions. There tended to be a wider range of frequencies near the middle of the HF band during the day and a narrower range of lower frequencies available during the night, especially during the fall when ionospheric electron density tended to be low. The spectrum monitor results revealed that there were plenty of unoccupied and nonforbidden frequencies available at all times. This means that ionospheric conditions were more of a limiting factor for the FMS than the spectrum monitor results. Overall, the successful merging of the results of the environmental monitor and spectrum monitor showed that there were sufficient frequencies available for OTHR operation during most times in this demonstration with decreased availability during the fall night and for the farthest two targets at Ulukhaktok and Alert. While this novel real-time FMS designed for high-latitude regions does not capture the true complexity of real-time operations, it could be used in conjunction with other tools to provide frequency guidance for operational scenarios.

Acknowledgment

The development of A-CHAIM is supported by Defense Research and Development Canada (contract number W7714-217622/001/SL) and is maintained by the Canadian High Arctic Ionospheric Network (CHAIN) with support from the Canadian Space Agency. This is Natural Resources Canada (NRCan) publication number 20210672.

References

[1] J. M. Headrick and M. I. Skolnik, "Over-the-horizon radar in the HF band," *Proc. IEEE*, vol. 62, no. 6, pp. 664–673, Jun. 1974.

[2] T. Thayaparan and J. MacDougall, "Evaluation of ionospheric sporadic-E clutter in an Arctic environment for the assessment of high-frequency surface-wave radar surveillance," *IEEE Trans. Geosci. Remote Sens.*, vol. 43, no. 5, pp. 1180–1188, May 2005.

[3] T. Thayaparan, Y. Ibrahim, J. Polak, and R. Riddolls, "High-frequency over-the-horizon radar in Canada," *IEEE Geosci. Remote Sens. Lett.*, vol. 15, no. 11, pp. 1700–1704, Nov. 2018.

[4] G. F. Earl and B. D. Ward, "The frequency management system of the Jindalee over-the-horizon backscatter HF radar," *Radio Sci.*, vol. 22, no. 2, pp. 275–291, Mar./Apr. 1987.

[5] T. A. Soame and R. K. Jarrott, "Architecture of an HF skywave radar network," in *Proc. 6th Int. Conf. HF Radio Syst. Techn.*, Jul. 1994, pp. 253–257.

[6] S. Maresca, P. Braca, J. Horstmann, and R. Grasso, "A network of HF surface wave radars for maritime surveillance: Preliminary results in the German bight," in *Proc. IEEE Int. Conf. Acoust., Speech Signal Process. (ICASSP)*, May 2014, pp. 6077–6081.

[7] K.-W. Gurgel, G. Antonischki, H.-H. Essen, and T. Schlick, "Wellen Radar (WERA): A new ground-wave HF radar for ocean remote sensing," *Coast. Eng.*, vol. 37, nos. 3–4, pp. 219–234, Aug. 1999.

[8] P. Moo, A. M. Ponsford, D. Difilippo, R. Mckerracher, N. Kashyap, and Y. Allard, "Canada's third generation high frequency surface wave radar system," *J. Ocean Technol.*, vol. 10, no. 2, pp. 21–28, 2015.

[9] A. L. Saverino, A. Capria, F. Berizzi, M. Martorella, and E. D. Mese, "Frequency management in HF-OTH skywave radar: Ionospheric propagation channel representation," *Prog. Electromagn. Res. B*, vol. 50, pp. 97–111, 2013.

[10] L.-W. Li, "High-frequency over-the-horizon radar and ionospheric backscatter studies in China," *Radio Sci.*, vol. 33, no. 5, pp. 1445–1458, Sep. 1998.

[11] V. Bazin *et al.*, "A general presentation about the OTH-radar NOSTRADAMUS," in *Proc. IEEE Conf. Radar*, May 2006, p. 9.

[12] R. J. Riddolls, "High-latitude application of three-dimensional over-the-horizon radar," *IEEE Aerosp. Electron. Syst. Mag.*, vol. 32, no. 12, pp. 36–43, Dec. 2017.

[13] M. Fagre, B. S. Zossi, J. Chum, E. Yiğit, and A. G. Elias, "Comparative study of equatorial and high-latitude over-the-horizon radar parameters using ray-tracing simulations," *IEEE Geosci. Remote Sens. Lett.*, vol. 18, no. 1, pp. 53–57, Jan. 2021.

[14] R. D. Hunsucker and J. K. Hargreaves, *The High-Latitude Ionosphere and its Effects on Radio Propagation*. Cambridge, U.K.: Cambridge Univ. Press, 2003.

[15] K. Davies, *Ionospheric Radio* ((IEE Electromagnetic Wave Series). London, U.K.: Peter Peregrinus, 1990.

[16] K. G. Budden, *The Propagation of Radio Waves: The Theory of Radio Waves of Low Power in the Ionosphere and Magnetosphere*. Cambridge, U.K.: Cambridge Univ. Press, 1985.

[17] K. Hocke and K. Schlegel, "A review of atmospheric gravity waves and travelling ionospheric disturbances: 1982–1995," *Ann. Geophys.*, vol. 14, no. 9, pp. 917–940, 1996.

[18] T. Thayaparan, E. M. Warrington, A. J. Stocker, and D. R. Siddle, "Simulation of the effect of convecting patches of enhanced electron density on HF over-the-horizon radars (OTHRs) in the polar regions," *IEEE Geosci. Remote Sens. Lett.*, vol. 18, no. 9, pp. 1570–1574, Sep. 2021.

[19] J. W. MacDougall, P. T. Jayachandran, and J. M. C. Plane, "Polar cap sporadic-E: Part 1, observations," *J. Atmos. Solar-Terr. Phys.*, vol. 62, no. 13, pp. 1155–1167, Sep. 2000.

[20] J. W. MacDougall, J. M. C. Plane, and P. T. Jayachandran, "Polar cap sporadic-E: Part 2, modeling," *J. Atmos. Solar-Terr. Phys.*, vol. 62, no. 13, pp. 1169–1176, Sep. 2000.

[21] T. G. Cameron, R. A. D. Fiori, D. R. Themens, E. M. Warrington, T. Thayaparan, and D. Galeschuk, "Evaluation of the effect of sporadic-E on high frequency radio wave propagation in the Arctic," *J. Atmos. Solar-Terr. Phys.*, vol. 228, Feb. 2022, Art. no. 105826.

[22] D. Bilitza *et al.*, "International Reference Ionosphere 2016: From ionospheric climate to real-time weather predictions," *Space Weather*, vol. 15, no. 2, pp. 418–429, Feb. 2017.

[23] B. Nava, P. Coïsson, and S. Radicella, "A new version of the NeQuick ionosphere electron density model," *J. Atmos. Solar-Terr. Phys.*, vol. 70, no. 15, pp. 1856–1862, Dec. 2008.

[24] P. Coïsson, S. M. Radicella, R. Leitinger, and B. Nava, "Topside electron density in IRI and NeQuick: Features and limitations," *Adv. Space Res.*, vol. 37, no. 5, pp. 937–942, Jan. 2006.

[25] D. R. Themens, P. T. Jayachandran, M. J. Nicolls, and J. W. MacDougall, "A top to bottom evaluation of IRI 2007 within the polar cap," *J. Geophys. Res., Space Phys.*, vol. 119, no. 8, pp. 6689–6703, Aug. 2014.

[26] T. Thayaparan, J. Marchioni, A. Kelsall, and R. Riddolls, "Improved frequency monitoring system for sky-wave over-the-horizon radar in Canada," *IEEE Geosci. Remote Sens. Lett.*, vol. 17, no. 4, pp. 606–610, Apr. 2020.

[27] D. R. Themens, B. Reid, A. M. McCaffrey, and P. T. Jayachandran, "The assimilation Canadian high Arctic ionospheric model (A-CHAIM): Implementation, workflow, and performance," Defence Res. Develop. Canada Ottawa Res. Centre, Nepean, ON, Canada, Tech. Rep. DRDC-RDDC-2020-C045, 2020.

[28] D. R. Themens, P. T. Jayachandran, A. M. McCaffrey, B. Reid, and R. H. Varney, "A bottomside parameterization for the empirical Canadian high Arctic ionospheric model," *Radio Sci.*, vol. 54, no. 5, pp. 397–414, May 2019.

[29] D. R. Themens, P. T. Jayachandran, I. Galkin, and C. Hall, "The empirical Canadian high Arctic ionospheric model (E-CHAIM): $N_m F_2$ and $h_m F_2$," *J. Geophys. Res., Space Phys.*, vol. 122, pp. 9015–9031, Aug. 2017.

[30] D. R. Themens *et al.*, "Topside electron density representations for middle and high latitudes: A topside parameterization for E-CHAIM based on the NeQuick," *J. Geophys. Res. Space Phys.*, vol. 123, pp. 1603–1617, Feb. 2018.

[31] B. Reid, D. R. Themens, A. M. McCaffrey, P. T. Jayachandran, M. G. Johnsen, and T. Ulich, "A-CHAIM: Near-real-time data assimilation of the high latitude ionosphere with a particle filter," *Earth Space Sci. Open Arch.*, 2022. [Online]. Available: https://www.essoar.org/doi/10.1002/essoar.10511639.1

[32] RFSPACE. (Oct. 2014). *SpectraVue User Guide, Version 3.18*. [Online]. Available: http://www.moetronix.com/files/spectravue.pdf

[33] C. Bianchi and A. Meloni, "Natural and man-made terrestrial electromagnetic noise: An outlook," *Ann. Geophys.*, vol. 50, no. 3, pp. 1–11, Dec. 2009.

[34] M. J. Ready, M. L. Downey, and L. J. Corbalis, "Automatic noise floor spectrum estimation in the presence of signals," in *Proc. Conf. Rec. 31st Asilomar Conf. Signals, Syst. Comput.*, vol. 1, Nov. 1997, pp. 877–881.

[35] B. Chan, "In-band and wideband frequency monitoring algorithms for DRDC over-the-horizon radar," Defence Res. Develop. Canada Ottawa Res. Centre, Nepean, ON, Canada, Tech. Rep. DRDC-RDDC-2017-R042, 2017.

[36] B. Chan, T. Thayaparan, and K. Shimotakahara, "Merging the frequency monitoring system with the ionospheric condition monitoring system for over the horizon radar," Defence Res. Develop. Canada Ottawa Res. Centre, Nepean, ON, Canada, Tech. Rep. DRDC-RDDC-2017-R158, 2018.

[37] D. R. Themens, P. T. Jayachandran, and A. M. McCaffrey, "Validating the performance of the empirical Canadian high Arctic ionospheric model (E-CHAIM) with *in situ* observations from DMSP and CHAMP," *J. Space Weather Space Climate*, vol. 9, p. A21, p. 14, Jun. 2019.

[38] D. R. Themens, P. T. Jayachandran, B. Reid, and A. M. McCaffrey, "The limits of empirical electron density modeling: Examining the capacity of E-CHAIM and the IRI for modeling intermediate (1- to 30-day) timescales at high latitudes," *Radio Sci.*, vol. 55, no. 4, pp. 1–15, Apr. 2020.

[39] C. Watson, D. R. Themens, and P. T. Jayachandran, "Development and validation of precipitation enhanced densities for the empirical Canadian high Arctic ionospheric model," *Space Weather*, vol. 19, no. 10, Oct. 2021, Art. no. e2021SW002779.

[40] D. R. Themens, B. Reid, C. Watson, A. M. McCaffrey, J. Bernard, and P. T. Jayachandran, "Implementation of particle precipitation into assimilation Canadian high Arctic ionospheric model (A-CHAIM) and a quiet D-Region in Empirical (E-CHAIM): Final report," Defence Res. Develop. Canada Ottawa Res. Centre, Nepean, ON, Canada, Tech. Rep. DRDC-RDDC-2021-C067, 2021.

[41] E. M. Warrington, "ADSA OTHR HIPLAB software toolbox," Defence Res. Develop. Canada Ottawa Res. Centre, Nepean, ON, Canada, Tech. Rep. W1410-195005/001/EE, 2019.

[42] N. Y. Zaalov, E. M. Warrington, and A. J. Stocker, "Simulation of off-great circle HF propagation effects due to the presence of patches and arcs of enhanced electron density within the polar cap ionosphere," *Radio Sci.*, vol. 38, no. 3, p. 1052, Jun. 2003.

[43] N. Y. Zaalov, E. M. Warrington, and A. J. Stocker, "A ray-tracing model to account for off–great circle HF propagation over northerly paths," *Radio Sci.*, vol. 40, no. 4, Aug. 2005, Art. no. RS4006.

[44] E. M. Warrington, N. Y. Zaalov, J. S. Naylor, and A. J. Stocker, "HF propagation modeling within the polar ionosphere," *Radio Sci.*, vol. 47, no. 4, pp. 1–7, Aug. 2012.

[45] E. M. Warrington *et al.*, "Near real-time input to a propagation model for nowcasting of HF communications with aircraft on polar routes," *Radio Sci.*, vol. 51, no. 7, pp. 1048–1059, Jul. 2016.

[46] R. M. Jones and J. J. Stephenson, *A Versatile Three-Dimensional Ray Tracing Computer Program for Radio Waves in the Ionosphere*. Washington, DC, USA: U.S. Department of Commerce, 1975.

[47] T. Thayaparan, D. Dupont, Y. Ibrahim, and R. Riddolls, "High-frequency ionospheric monitoring system for over-the-horizon radar in Canada," *IEEE Trans. Geosci. Remote Sens.*, vol. 57, no. 9, pp. 6372–6384, Sep. 2019.

[48] S. Henault and G. A. Morin, "Null-steering sensitivity to ground properties in over-the-horizon radar with planar monopole array on finite radial ground plane," in *Proc. IEEE Int. Symp. Antennas Propag. USNC/URSI Nat. Radio Sci. Meeting*, Jul. 2018, pp. 2149–2150.

[49] *Radio Noise: P Series Radiowave Propagation. Part 6: Man-Made Noise*, document ITU-R P.372-15, International Telecommunication Union, Sep. 2019.
[50] T. Thayaparan, M. Warrington, A. Stocker, and D. Siddle, "Effect of frequency monitoring system for over-the-horizon radar due to the presence of patches and arcs within the polar cap ionosphere," in *Proc. 21st Int. Radar Symp. (IRS)*, Oct. 2020, pp. 368–372.
[51] J. J. Ruck and D. R. Themens, "Impacts of auroral precipitation on HF propagation: A hypothetical over-the-horizon radar case study," *J. Atmos. Solar-Terr. Phys.*, vol. 19, no. 12, Dec. 2021, Art. no. e2021SW002901.
[52] S. Henault and G. A. Morin, "Cross-polarized null-steering in over-the-horizon radar with planar monopole array on finite radial ground plane," in *Proc. IEEE Int. Symp. Antennas Propag. USNC/URSI Nat. Radio Sci. Meeting*, Jul. 2018, pp. 2151–2152.
[53] S. Henault and R. J. Riddolls, "Investigation of a 256-monopole transmit antenna array for over-the-horizon radar in Canada," *Radio Sci.*, vol. 54, no. 10, pp. 888–903, Oct. 2019.

Thayananthan Thayaparan (Senior Member, IEEE) received the B.Sc. degree (Hons.) in physics from the University of Jaffna, Jaffna, Sri Lanka, in 1986, the M.Sc. degree in physics from the University of Oslo, Oslo, Norway, in 1991, and the Ph.D. degree in atmospheric physics from the University of Western Ontario, London, ON, Canada, in 1996.

From 1996 to 1997, he was employed as a Post-Doctoral Fellow with the University of Western Ontario. In 1997, he joined the Defense Research and Development Canada-Ottawa, Department of National Defense, as a Defense Scientist. His research includes ionospheric modeling for over-the-horizon radar (OTHR), synthetic aperture radar imaging algorithms, time–frequency analysis for radar imaging and signal analysis, radar micro-Doppler analysis, and noise radar technology. He has authored or coauthored over 230 publications in journals, proceedings, and internal distribution reports.

Dr. Thayaparan is a Fellow of the Institute of Engineering and Technology (IET). He is currently serving on the Editorial Board of IET Signal Processing. He was a recipient of the IET Premium Award for Signal Processing for the best paper published in 2009–2010. As a Principal Writer, he wrote five editorials for the international journals *IET Signal Processing* and *IET Radar, Sonar and Navigation*. He coauthored a textbook entitled *Time-Frequency Signal Analysis with Applications*.

Hannah Villeneuve, photograph and biography not available at the time of publication.

David R. Themens, photograph and biography not available at the time of publication.

Benjamin Reid, photograph and biography not available at the time of publication.

Michael Warrington, photograph and biography not available at the time of publication.

Taylor Cameron, photograph and biography not available at the time of publication.

Robyn Fiori, photograph and biography not available at the time of publication.